Atmospheric
Chemistry
and Physics

Supplement of

Improved calculation of single-scattering properties of frozen droplets and frozen-droplet aggregates observed in deep convective clouds

Jeonggyu Kim et al.

Correspondence to: Junshik Um (jjunum@pusan.ac.kr)

S1. Aggregates of Gaussian random spheres

The best-fit model of a single Gaussian random sphere is presented in Fig. 7. Using this model, a total 27 aggregates of Gaussian random spheres were constructed. These aggregates consist of homogeneous components (ranging from 2 to 10) of identical size and exhibit a variety of 3D morphologies (i.e., varying AI), spanning from compact forms to linearly chained structures (see Section 4.2).

Figure S1 illustrates the P_{11} and g at $\lambda = 0.80$ μm for 27 aggregates of Gaussian random spheres (depicted by blue shaded area), which show an average difference of 1.02 ± 0.55 %, 18.49 ± 5.08 %, and 2.86 ± 2.05 % from the in-situ measurements in the forward-, lateral-, and backward-scattering regions, respectively. A notable observation is that the discrepancies in the lateral-scattering region, which were apparent in the individual Gaussian random sphere models, are also present in the aggregates of Gaussian random sphere models (see Figs. S1a and S4). These discrepancies persist, and in some cases, are exacerbated due to the interactions among the components within the FDAs (See Fig. S3).

Figure S1b shows how the calculated g varies as a function of the number of Gaussian random spheres within the aggregates. Generally, an increase in the number of components in the FDAs corresponds to a decrease in g. This is attributed to the fact that a higher number of chained FDs leads to an extended path length for reflected and refracted rays, thereby decreasing the scattered energy in the forward-scattering region. Despite this, the g value remains slightly higher than the average in situ measurement (i.e., 0.78).

Figure S2 shows the impact of varying the t on the results for (a) ω, (b) RMSE, and (c) g, with t values ranging from 0.0 to 0.95, in increments of 0.05. The ω values initially increase with t increases, peaking at 24 when $t = 0.55$. Beyond this point, ω begins to decline as excessive distortion flattens P_{11} in both the lateral- and backward-scattering regions. The RMSE minimizes at 0.0795 when $t = 0.55$, but starts to increase significantly as t exceeds this value. The g value remains relatively stable up to $t = \sim 0.35$, after which it steadily declines due to reduced forward-scattered intensities caused by higher distortion. At $t = 0.45$, the average $\pm$ standard deviation of the computed g values is 0.78 ± 0.01, which falls within the range of PN measurements (0.78 ± 0.04).

Figure S3 shows the variations in the differences in the lateral-scattering region of P_{11} relative to in situ measurements across the range of t values from 0.0 to 0.95. As indicated in Fig. S2, as the number of components in an FDAs model increases, the discrepancy between the model and observations tends to grow. More detailed statistics of differences across the three different scattering regions as a function of distortion parameters are provided in Table S1.

Figure S4 shows the P_{11} for homogeneous aggregates of Gaussian random spheres that yielded the smallest RMSE with t values from 0.0 to 0.95. The best-fit model, consisting of 3 Gaussian random spheres from case 4 (i.e., (d) in Fig. 1), minimized the RMSE to 0.0795 when $t = 0.55$ was applied. The P_{11} for this model shows a relative difference of -0.34 %, +8.26 %, and -3.58 % in the forward-, lateral-, and backward-scattering regions, respectively. While the best-fit model improved the agreement in the forward-scattering region compared to the single Gaussian random sphere model, it did not achieve better agreement in the lateral-scattering region due to the multiple scattering effects among the components and the flattening of P_{11} induced by a high t. The g was 0.78, which falls within the PN uncertainty range.
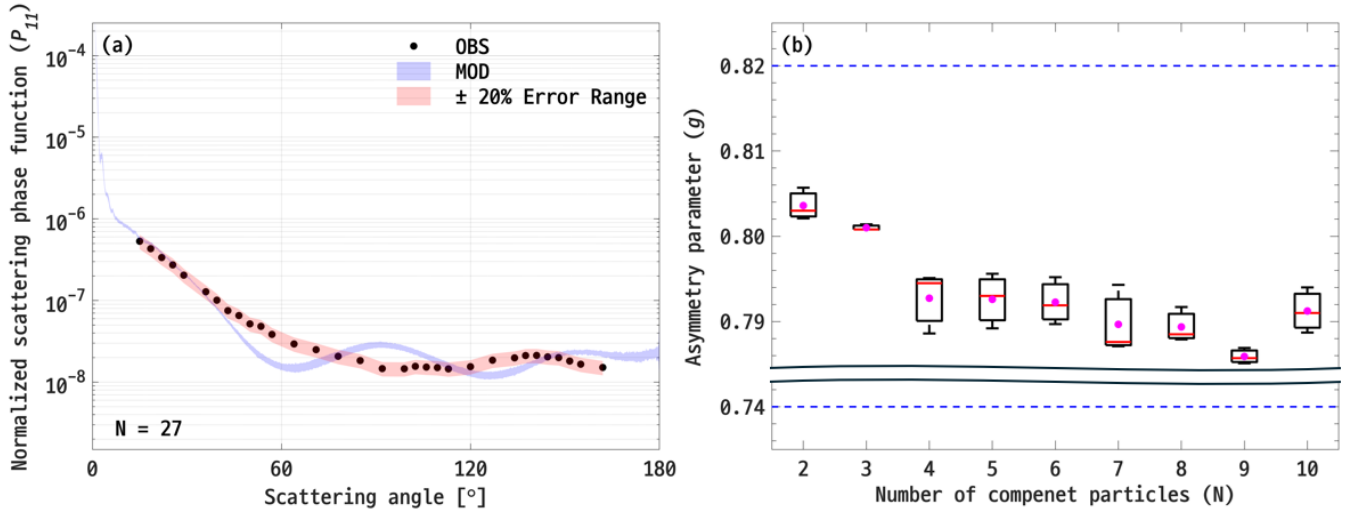
Figure S1. (a) The calculated P_{11} for FDAs represented by aggregates of Gaussian random spheres with $t = 0.0$ at $\lambda = 0.80$ µm. The filled black circles and a shaded red area represent the in situ measured P_{11} obtained during CIRCLE−2 and ±20% uncertainty range of PN instrument, respectively. The shaded blue area indicates the computed P_{11} for FDAs, and N denotes the total number of aggregates of Gaussian random spheres developed in this study. **(b)** The variation in computed g values as a function of the number of components. The solid red lines and dashed blue lines represent the median g value for each component count and uncertainty range for the g measured by PN, respectively. The filled magenta circles correspond to the mean of g.
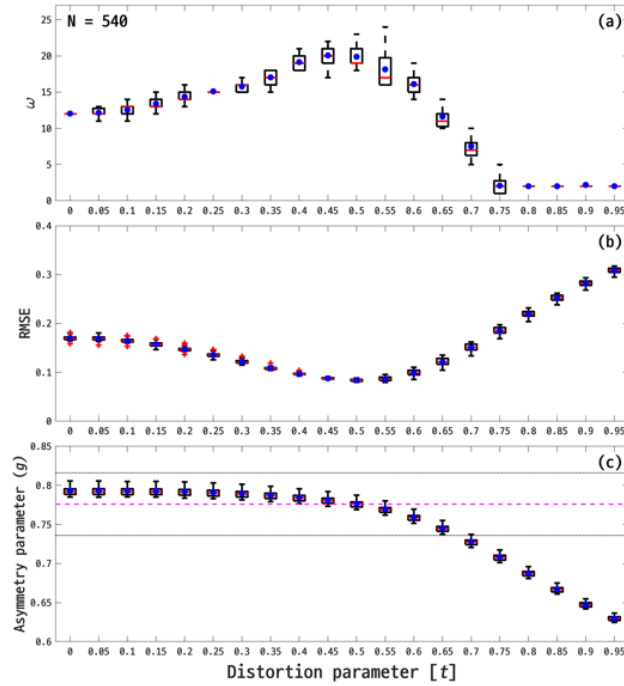

Figure S2. Results for aggregates of Gaussian random sphere models with t values ranging from 0.0 to 0.95 in 0.05 intervals, focusing on **(a)** ω, **(b)** RMSE, and **(c)** g. The solid red lines and filled blue circles represent the median and mean, respectively. The dotted black lines and dashed magenta line in panel (c) indicate the boundaries of the PN uncertainty range and the mean of PN measurements (i.e., 0.78 ± 0.04), respectively. The total number of simulated Gaussian random sphere models (N) is shown in the panel (a).
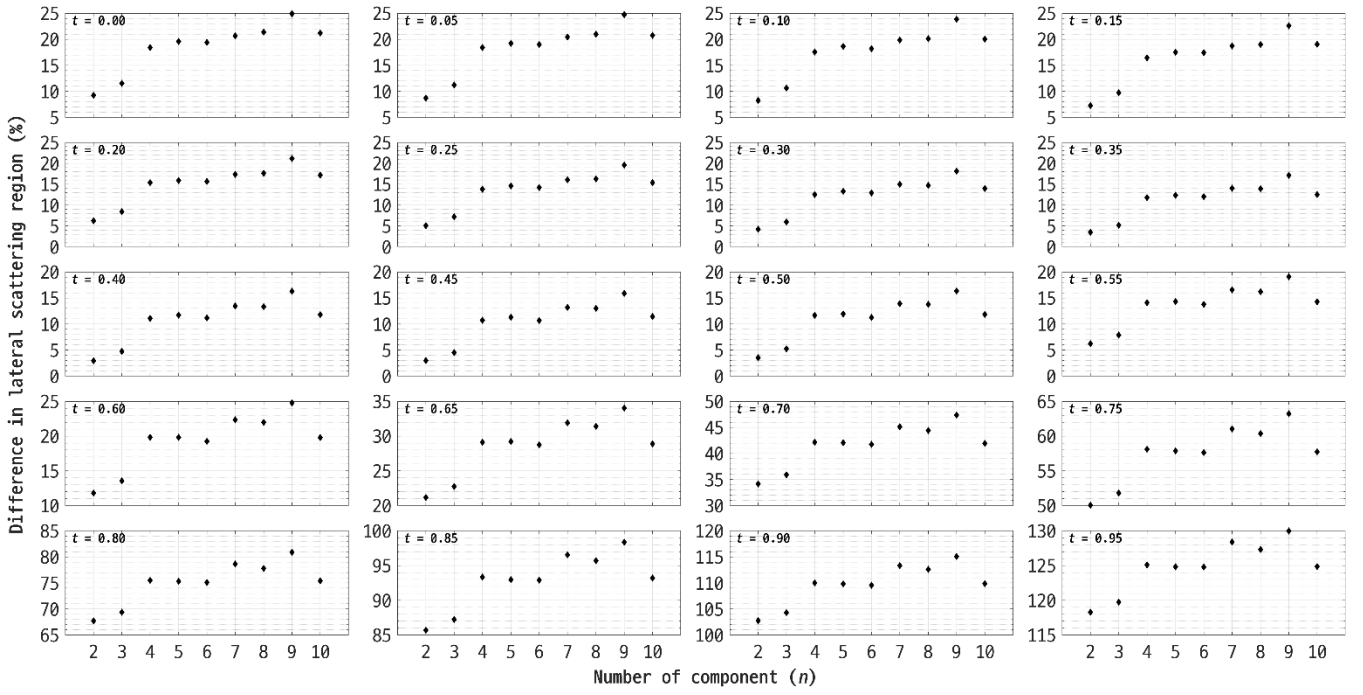
Figure S3. The differences in lateral-scattering region between the in situ measured P_{11} and computed P_{11} for the FDAs consisting of Gaussian random spheres. The corresponding distortion parameter (t) was shown on the upper-left side of each panel.
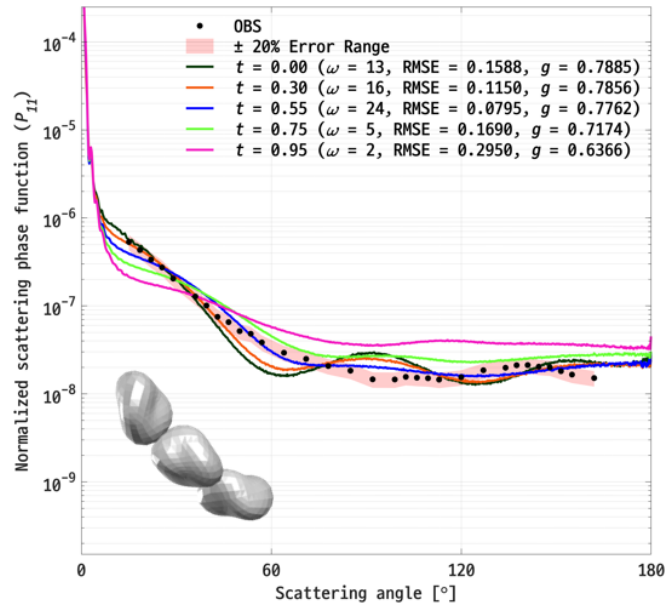
60

65

Figure S4. A comparison of the average in situ measured P_{11} (represented by filled black circles) with the calculated P_{11} of aggregates of Gaussian random sphere models. A shaded red area indicates the ±20% uncertainty range of the PN measurements, and each
70 **solid line corresponds to the best-fit model at t values ranging from 0.0 to 0.95 (not all lines are shown here for brevity). The t values for each best-fit line, along with the corresponding ω, RMSE, and g are shown on the upper-right side of the panel. The shape of the best-fit model is shown on the bottom-left of the panel.**

Table S1. The calculated average ± standard deviation of the difference (relative difference of the best-fit model) in P_{11}, compared
75 **to the PN measurements, for aggregates of Gaussian random spheres across the forward- (FWD), lateral- (LAT), and backward-**

(BWD) scattering regions. For *g*, the average ± standard deviation is shown, with the relative difference indicated in parentheses. The *t* values, ranging from 0.0 to 0.95 in 0.05 intervals, were applied.

t	FWD	LAT	BWD	g	t	FWD	LAT	BWD	g
0.00	1.02 ± 0.55% (-0.98%)	18.49 ± 5.08% (+19.80%)	2.86 ± 2.05% (+2.65%)	0.79 ± 0.01 (0.79, +1.61%)	0.05	0.99 ± 0.58% (-0.86%)	18.16 ± 5.13% (+19.35%)	2.86 ± 2.12% (+2.05%)	0.79 ± 0.01 (0.79, +1.65%)
0.10	0.90 ± 0.61% (-0.74%)	17.46 ± 5.01% (+18.73%)	2.86 ± 2.18% (+1.46%)	0.79 ± 0.01 (0.79, +1.64%)	0.15	0.83 ± 0.63% (-0.53%)	16.42 ± 4.91% (+17.88%)	3.14 ± 2.59% (-0.23%)	0.79 ± 0.01 (0.79, +1.65%)
0.20	0.80 ± 0.67% (-0.41%)	15.01 ± 4.80% (+16.88%)	4.01 ± 2.96% (-1.10%)	0.79 ± 0.01 (0.79, +1.52%)	0.25	0.82 ± 0.71% (-0.29%)	13.57 ± 4.68% (+15.99%)	5.03 ± 3.21% (-2.49%)	0.79 ± 0.01 (0.79, +1.37%)
0.30	0.84 ± 0.75% (-0.13%)	12.31 ± 4.57% (+14.72%)	6.02 ± 3.09% (-3.70%)	0.79 ± 0.01 (0.79, +1.24%)	0.35	0.83 ± 0.72% (-0.67%)	11.39 ± 4.49% (+17.12%)	6.61 ± 2.97% (-3.60%)	0.79 ± 0.01 (0.78, +0.72%)
0.40	0.80 ± 0.65% (+0.22%)	10.72 ± 4.39% (+11.13%)	6.69 ± 2.85% (-5.71%)	0.78 ± 0.01 (0.78, +1.02%)	0.45	0.76 ± 0.56% (+0.35%)	10.42 ± 4.29% (+9.50%)	6.06 ± 2.82% (-7.13%)	0.78 ± 0.01 (0.78, +0.89%)
0.50	0.91 ± 0.52% (+0.69%)	11.05 ± 4.29% (+4.38%)	4.18 ± 2.74% (-5.22%)	0.78 ± 0.00 (0.78, +0.80%)	0.55	1.61 ± 0.87% (-0.34%)	13.59 ± 4.26% (+8.26%)	2.19 ± 1.53% (-3.58%)	0.77 ± 0.00 (0.78, +0.03%)
0.60	3.41 ± 0.95% (-1.30%)	19.24 ± 4.32% (+9.85%)	6.69 ± 2.64% (+0.89%)	0.76 ± 0.00 (0.77, -0.82%)	0.65	6.02 ± 0.95% (-3.95%)	28.59 ± 4.38% (+19.12%)	16.17 ± 2.62% (+10.60%)	0.75 ± 0.00 (0.76, -2.69%)
0.70	9.35 ± 0.96% (-7.27%)	41.66 ± 4.47% (+32.25%)	27.90 ± 2.59% (+22.24%)	0.73 ± 0.00 (0.74, -4.99%)	0.75	13.20 ± 0.94% (-11.16%)	57.54 ± 4.48% (+48.22%)	41.12 ± 2.50% (+35.57%)	0.71 ± 0.00 (0.72, -7.55%)
0.80	17.40 ± 0.93% (−15.42%)	75.08 ± 4.44% (+65.94%)	55.43 ± 2.37% (+50.20%)	0.69 ± 0.00 (0.70, -10.30%)	0.85	21.73 ± 0.90% (-19.80%)	92.88 ± 4.35% (+83.84%)	70.30 ± 2.28% (+65.11%)	0.67 ± 0.00 (0.68, -13.00%)
0.90	25.99 ± 0.86% (−24.13%)	109.70 ± 4.21% (+101.08%)	85.29 ± 2.16% (+80.33%)	0.65 ± 0.00 (0.65, -15.61%)	0.95	29.98 ± 0.81% (-28.24%)	124.81 ± 3.99% (+116.83%)	100.06 ± 2.03% (+95.30%)	0.63 ± 0.00 (0.64, -17.96%)

80

85

90

95

100

S2. Aggregates of droxtals

The best-fit model of a single droxtal is presented in Fig. 10. Using this model, a total 27 aggregates of droxtals were constructed, consisting of homogeneous components (ranging from 2 to 10) of identical size with varying 3D morphologies (see Section 4.2).

Figure S5a compares the P_{11} for these aggregates of droxtals with in situ measurements at $\lambda = 0.80$ μm. In the forward-scattering region, pronounced peaks persist due to the faceted structure of droxtals (see Figs. 8 and 10). Consequently, droxtal aggregates with $t = 0.0$ exhibited relatively larger discrepancies in the forward-scattering region, with average differences of 5.19 ± 1.35 %, 4.98 ± 2.97 %, and 14.47 ± 2.61 % in the forward-, lateral-, and backward-scattering regions, respectively.

Figure S5b shows the variation in the calculated g as a function of the number of attached droxtals. The g values of the FDA models represented by droxtals exhibit a similar trend to those of Gaussian random sphere aggregates, with g decreasing as the number of components increases (see Fig. S1b). A detailed summary of the average differences and standard deviations for both P_{11} and g values of droxtal aggregates, across distortion parameters ranging from $t = 0.0$ to $t = 0.95$, is provided in Table S2.

Figure S6 displays box plots analyzing ω, RMSE, and g for aggregates of droxtal models with t ranging from 0.0 to 0.95 in 0.05 intervals. As expected from the results with single droxtals, increasing t causes the sharp peaks in the forward-scattering region of P_{11} to become smoother, reducing the differences between the models and PN measurements. This results in more observation angles falling within the PN uncertainty range. Overall, ω increases with t, reaching a peak of 31 at $t = 0.45$, before decreasing as higher t values flatten the lateral- and backward-scattering regions of P_{11}. In the forward-scattering region, ω shows a significant increase with t, starting from an average of 1.96 ± 0.52 out of 12 with no distortion, and rising to 11.96 ± 0.19 out of 12 at $t = 0.45$. Conversely, RMSE initially decreases, reaching its minimum at $t = 0.45$, but tends to increase with greater distortion. The g value is 0.78 at $t = 0.55$, effectively matching the PN measurements (0.78 ± 0.04).

Figure S7 illustrates that the difference in lateral-scattering between FDAs models represented by droxtals and in-situ measurements increases with the number of components. Additionally, it shows that this difference also grows as t increases. The statistical differences across the three scattering regions for varying distortion parameters are detailed in Table S2.

Figure S8 presents simulated P_{11} for droxtal aggregates, with each colored line representing the best-fit to the in situ measured P_{11} at different t values, ranging from 0.0 to 0.95. The best-fit model, consisting of aggregates of 8 droxtals of type 3 (see Fig. 3c), yielded a minimum RMSE of 0.0502 and a g value of 0.78 at $t = 0.45$. The differences of this best-fit model from the in situ measurements were -0.17 %, +6.09 %, and -0.14 % in the forward-, lateral-, and backward-scattering regions, respectively. This model effectively replicated the measurements not only in the lateral but also in the backward-scattering regions.
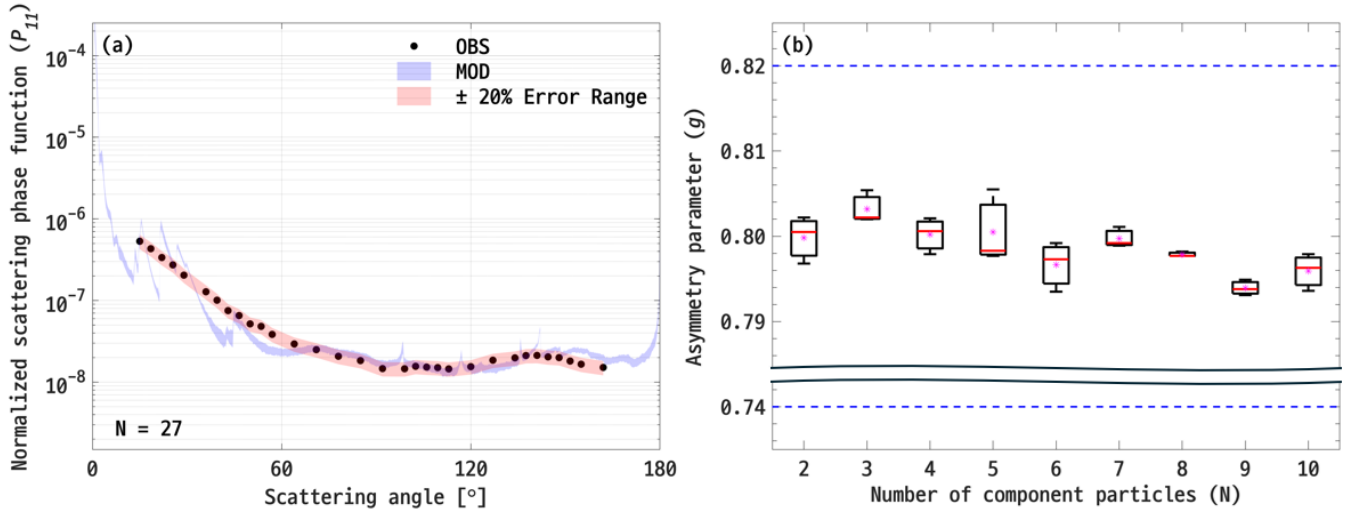
5

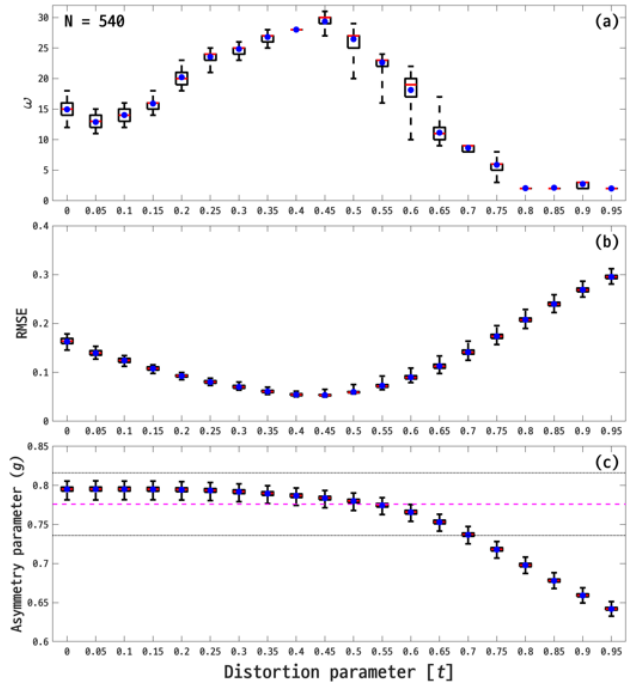**Figure S5. The same as Fig. S1 but for the aggregates of droxtals.**

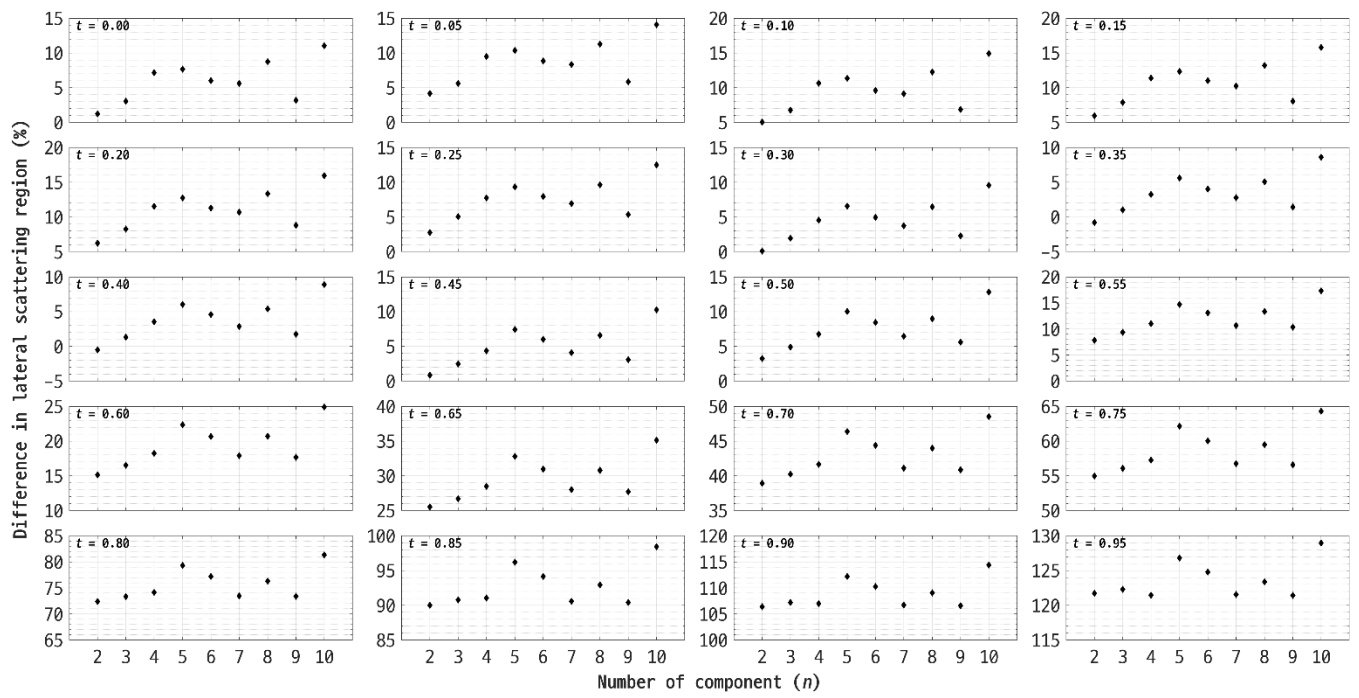**Figure S6. The same as Fig. S2 but for the aggregates of droxtals**

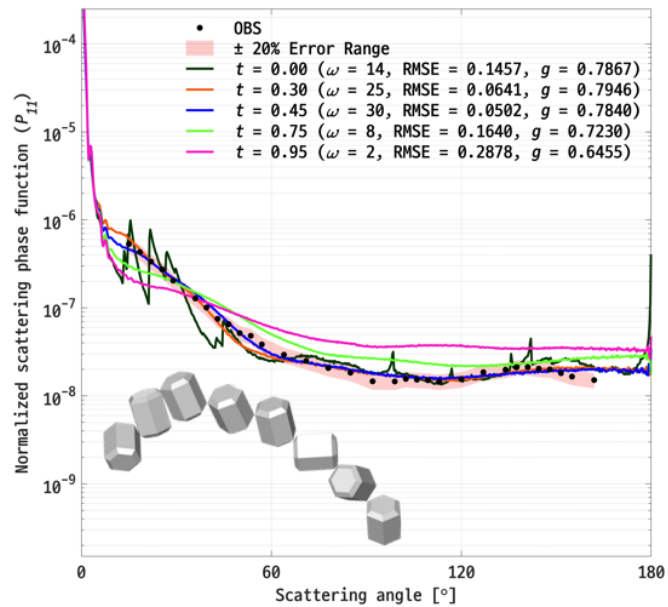**Figure S7. The same as Fig. S3 but for the aggregates of droxtals.**

160

165

170   **Figure S8. The same as Fig. S4 but for the aggregates of droxtals**

Table S2. The same as Table S1 bur for the aggregates of droxtals.

| t	FWD	LAT	BWD	g	t	FWD	LAT	BWD	g
0.00	5.26 ± 1.41% (+3.07%)	4.96 ± 3.39% (+11.73%)	14.79 ± 2.94% (+21.01%)	0.79 ± 0.00 (0.79, +1.38%)	0.05	1.48 ± 0.82% (-3.43%)	7.94 ± 3.78% (+16.54%)	18.14 ± 2.90% (+24.43%)	0.79 ± 0.00 (0.79, +1.34%)
0.10	1.66 ± 0.81% (-1.70%)	9.43 ± 3.69% (+9.78%)	19.26 ± 2.70% (+16.18%)	0.79 ± 0.00 (0.80, +2.77%)	0.15	1.89 ± 0.80% (-1.29%)	10.51 ± 3.55% (+7.44%)	19.22 ± 2.60% (+18.20%)	0.80 ± 0.00 (0.80, +2.65%)
0.20	1.65 ± 0.83% (-0.77%)	11.15 ± 3.45% (+8.27%)	17.86 ± 2.65% (+16.51%)	0.79 ± 0.00 (0.80, +2.63%)	0.25	0.65 ± 0.65% (-0.13%)	7.66 ± 3.40% (+4.50%)	11.81 ± 2.38% (+10.90%)	0.79 ± 0.00 (0.80, +2.44%)
0.30	0.63 ± 0.55% (+0.56%)	4.74 ± 3.07% (+3.54%)	5.87 ± 2.30% (+2.90%)	0.79 ± 0.00 (0.79, +2.40%)	0.35	0.79 ± 0.55% (+0.92%)	3.89 ± 3.13% (+2.39%)	2.47± 1.82% (-0.39%)	0.79 ± 0.00 (0.79, +2.09%)
0.40	0.69 ± 0.56% (-0.21%)	4.26 ± 3.21% (+6.06%)	1.67 ± 1.60% (+0.36%)	0.79 ± 0.00 (0.78, +1.15%)	0.45	0.55 ± 0.59% (-0.17%)	5.40 ± 3.53% (+6.09%)	1.92 ± 1.51% (-0.14%)	0.78 ± 0.00 (0.78, +1.03%)
0.50	0.67 ± 0.66% (-0.36%)	7.77 ± 3.76% (+6.52%)	2.13 ± 1.42% (-2.18%)	0.78 ± 0.00 (0.78, +0.66%)	0.55	1.55 ± 0.80% (-0.39%)	12.43 ± 3.84% (+6.99%)	1.74 ± 1.46% (-3.02%)	0.78 ± 0.00 (0.78, +0.30%)
0.60	3.22 ± 0.87% (-1.64%)	19.77 ± 3.95% (+13.32%)	3.06 ± 2.09% (-1.65%)	0.77 ± 0.00 (0.77, -0.58%)	0.65	5.76 ± 0.89% (-4.04%)	30.13 ± 4.05% (+23.26%)	9.99 ± 2.31% (+6.66%)	0.75 ± 0.00 (0.76, -2.24%)
0.70	8.98 ± 0.86% (-7.62%)	43.43 ± 4.17% (+37.07%)	20.26 ± 2.33% (+16.62%)	0.74 ± 0.00 (0.74, -4.36%)	0.75	12.74 ± 0.94% (-11.20%)	59.14 ± 4.22% (+53.02%)	32.74 ± 2.28% (+29.23%)	0.72 ± 0.00 (0.72, -6.83%)
0.80	16.79 ± 0.84% (-15.55%)	76.20 ± 4.32% (+69.99%)	46.74 ± 2.54% (+42.61%)	0.70 ± 0.00 (0.70, -9.46%)	0.85	20.84 ± 0.86% (-19.66%)	93.29 ± 4.06% (+87.75%)	60.91 ± 2.59% (+57.01%)	0.68 ± 0.00 (0.68, -11.30%)
0.90	24.84 ± 0.74% (-23.88%)	109.08 ± 4.01% (+104.33%)	75.02 ± 2.74% (+70.37%)	0.66 ± 0.00 (0.66, -14.55%)	0.95	28.63 ± 0.76% (-27.65%)	124.16 ± 3.69% (+119.66%)	88.63 ± 2.64% (+83.44%)	0.64 ± 0.00 (0.65, -16.06%)

175

180

185

190

195

S3. A weighted habit mixture model

200 A weighted habit mixture model (i.e., indirect method) was constructed using the components of model D from Fig. 11d to assess whether similar results to those obtained from the directly aggregated habit mixture models developed in this study could be achieved. The P_{11} and g of the components were weighted following the method of Baran et al. (2012) (see their Eq. (3)). The weighted P_{11} is given by

$$P_{11(best-fit)} = c1P_{11(GS,t=0.3)} + c2P_{11(DX,t=0.3)}, \qquad (S1)$$

205 where c1 and c2 are the weights applied to each P_{11}, and their sum equals 1. The distortion parameter (t) applied to these component models was set to 0.3 because model D minimized RMSE at $t = 0.3$ (as discussed in Sect 4.3.). The best weighted mean habit mixture model was identified with c1 = 0.14 and c2 = 0.86. This habit mixture (see Fig. S9) exhibited differences in the forward-, lateral-, and backward-scattering regions of +3.58 %, -12.83 %, and +2.06 %, respectively. The ω was 18 out of 32, closely matching the lateral-scattering region (i.e., $\omega = 9$ out of 11), but showing relatively poor agreement in the

210 forward- and backward-scattering regions (i.e., $\omega = 3$ out of 12 and $\omega = 6$ out of 9, respectively). The RMSE was 0.1119, which is higher than that of directly aggregated habit mixture models (see Fig. 11). The g value was 0.82, which is close to the upper range of PN measurements. These comparison results suggest that directly constructed habit mixture models more accurately simulate the in situ measurements than those developed using the indirect method, as well as single-particle models and aggregates models consisting of homogeneous components.

215
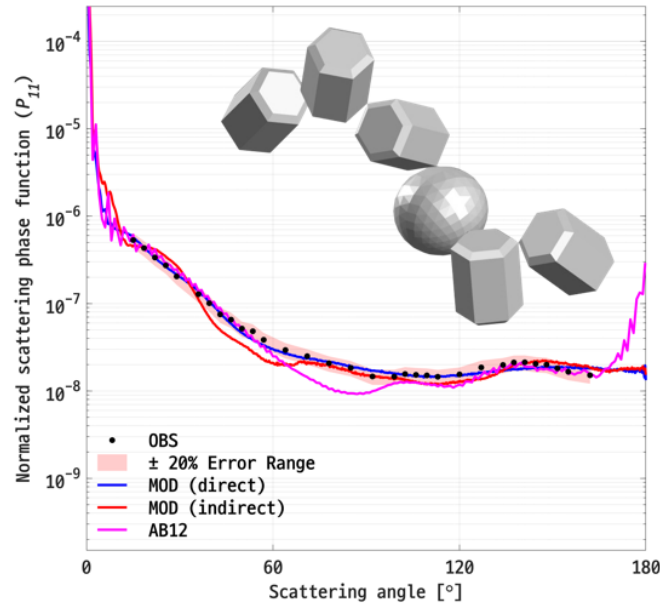
Figure S9. Shape and P_{11} of habit mixture models. The P_{11} of the habit mixture model with directly aggregated components is represented by a solid blue line, while the one constructed using the indirect method (i.e., by weighting) is shown as a solid red line. The P_{11} of the weighted habit mixture model developed by Baran et al. (2012) (AB12, solid magenta line) and the PN measurements
220 **(filled black circles) with their uncertainty range (shaded red area) are also shown."**

225